Check for updates

Advanced Energy Materials

ADVANCED ENERGY MATERIALS
www.advenergymat.de

RESEARCH ARTICLE OPEN ACCESS

Compositional Tuning and Surface Restructuring Synergistically Enhance Perovskite Ferrite Catalysts for Hydrogen Evolution in a Membrane-Less Electrolyzer

Yixin Bi[1] | Yuhao Wang[1] | Zilong Wang[1] | Yufei Song[4] | Nuotong Li[1] | Jingwei Li[2,3] | Arini Kar[2,3] | Qing Chen[1] | Francesco Ciucci[1,2,3]

[1]Department of Mechanical and Aerospace Engineering, The Hong Kong University of Science and Technology, Kowloon, Hong Kong SAR, China | [2]Chair of Electrode Design for Electrochemical Energy Systems, University of Bayreuth, Bayreuth, Germany | [3]Bavarian Center for Battery Technology (BayBatt), University of Bayreuth, Bayreuth, Germany | [4]State Key Laboratory of Materials-Oriented Chemical Engineering, College of Chemical Engineering, Nanjing Tech University, Nanjing, China

Correspondence: Qing Chen (chenqing@ust.hk) | Francesco Ciucci (francesco.ciucci@uni-bayreuth.de)

Received: 27 September 2025 | **Revised:** 24 January 2026 | **Accepted:** 28 January 2026

Keywords: hydrogen evolution reaction | membrane-less electrolyzer | perovskite catalyst | surface restructuring | water electrolysis

ABSTRACT

Balancing stability and activity of the hydrogen evolution reaction (HER) electrocatalysis remains challenging for advanced electrolysis technologies. This work introduces a synergistic design strategy to tackle the challenge with in situ surface restructuring. Fe-based double perovskite is developed with an optimal electronic structure for HER catalysis, delivering an overpotential of 325 mV in 0.1 M KOH and 184 mV in 1 M KOH at 10 mA/cm^2, among the best reported. Additionally, the catalyst exhibited remarkable self-improving stability, with specific activity increasing 1.98 times at 300 mV overpotential after 20 h, due to the restructuring of an amorphous layer confirmed with transmission electron microscopy. To demonstrate practical utility, the catalyst was integrated into an active flow membraneless electrolyzer (AFME), a promising technology that is currently limited by instability. The device demonstrated outstanding operational stability for 1000 h at 50 mA/cm^2, with a minimal decay rate of 0.25 mV/h, establishing a new benchmark for membraneless systems. This work not only presents a powerful strategy for designing self-improving catalysts but also validates its practical efficacy in next generation electrolyzer technologies, paving the way for cost-effective green hydrogen production.

1 | Introduction

The large-scale production of green hydrogen via water electrolysis requires the development of active and stable electrocatalysts made from earth-abundant materials. Although many highly active catalysts have been identified, their long-term stability continues to be a major obstacle for real-world use. A significant challenge lies in balancing long-term stability with high catalytic activity [1]. For instance, CoP is active for hydrogen evolution catalysis but unstable because it transforms to (oxy)phosphates in 20 min [2]. Highly active Co-MoS_2 undergoes dissolution to form MoO_4^{2-} and SO_3^{2-} in alkaline conditions, thus degrading its stability [1]. Schalenbach et al. [3] showed that Ni-Mo alloys are effective for hydrogen evolution but experience Mo leaching into the electrolyte during HER conditions. Zhai et al. [4] demonstrated that HER-active precious metal catalysts, such as Pt, Ru, Pd, Rh, and Ir-based composites, also experience agglomeration or loss of their active metals in alkaline environments, which then

This is an open access article under the terms of the Creative Commons Attribution License, which permits use, distribution and reproduction in any medium, provided the original work is properly cited.

© 2026 The Author(s). *Advanced Energy Materials* published by Wiley-VCH GmbH

compromises their stability. Addressing or rethinking the issue of degradation is essential for developing truly durable and effective HER catalysts.

Among various material options, transition metal perovskite oxides are promising candidates due to their compositional versatility. Specifically, Fe-based transition metal perovskite oxides are attractive due to affordability. However, the role of Fe has mostly been as a substitutional defect into Co- and Ni-based perovskites, owing to their generally lower intrinsic activity [5, 6], such as $SrNb_{0.1}Co_{0.7}Fe_{0.2}O_{3-\delta}$ [7], $Pr_{0.5}(Ba_{0.5}Sr_{0.5})_{0.5}Co_{0.8}Fe_{0.2}O_{3-\delta}$ [8], and $SrCo_{0.7}Fe_{0.25}Mo_{0.05}O_{3-\delta}$ [9]. There are limited works focusing on improving the activity of Fe-based perovskites for HER catalysis through doping or morphology design [10–13]. However, the reported activity remains inadequate, and their synthesis methods, such as the colloidal crystal template method or ammonolysis, are intricate. Furthermore, they didn't consider the issue of HER stability, with limited stability test time and a lack of in-depth discussion about the HER stability mechanism. Thus, a comprehensive design considering both activity and stability for the HER catalyst is urgently required.

This work presents an approach that repurposes the usually destructive elemental loss as a means for in situ self-enhancement to tackle both activity and stability challenges. By designing a catalyst that experienced surface restructuring during stability operation, we induced the development of a more active and stable amorphous surface layer. In a 20 h' stability operation, the material formed an amorphous surface layer that enhanced its specific activity by 1.98 fold.

To demonstrate the long-term reliability of the catalyst, we use emerging active flow membraneless electrolyzers (AFMEs) as a platform. The removal of a membrane and the simple system design reduce the cost of green hydrogen production. However, most existing AFMEs employ precious metals (such as Pt) for the electrodes [14–21], which increases costs. Furthermore, the stability of AFME is often overlooked; many studies have developed new types of AFME, but have not conducted stability tests [17, 18, 22, 23], with the longest stability test reported only 250 h [24]. By integrating our robust catalyst into a custom-fabricated AFME, we demonstrated the tangible benefits of our materials design strategy in a practical device, ultimately achieving an operational lifetime of 1000 h at 50 mA/cm^2, with a minimal voltage decay rate of 0.25 mV/h. This duration significantly surpasses previously reported stability tests for this class of electrolyzers.

2 | Experimental Section

2.1 | Synthesis of Perovskite Powders

All the perovskite powders were synthesized using the sol-gel method. Stoichiometric amounts of $C_4H_6O_4Ba$, $Nd(NO_3)_3{\cdot}6H_2O$, and $Fe(NO_3)_3{\cdot}9H_2O$ were dissolved in deionized water. Subsequently, ethylenediaminetetraacetic acid (EDTA) and citric acid (CA) were incorporated into the solution at a molar ratio of metal ion: EDTA:CA of 1:1:2, with ammonia used to adjust the pH to 7. The solution was heated and stirred to form the gel; subsequent drying of the gel at 250°C resulted in the formation of the solid precursors. The perovskite powders were then synthesized by calcining the aforementioned precursor at 1000°C for 10 h.

2.2 | Preparation of the Working Electrode

A mixture of 10 mg of perovskite powder, 10 mg of Vulcan XC72, and 100 µL of 5 wt. % Nafion solution was combined with 1000 µL of ethanol. This blend was ultrasonically dispersed for 1 h to form the catalyst ink. Then, 5 µL of this catalyst ink was deposited onto the surface of a polished glassy carbon electrode (4 mm in diameter) and dried at room temperature for 30 min.

2.3 | Electrochemical Measurements

The HER performance of perovskite powders was evaluated using a standard three-electrode system consisting of a (KCl-saturated) Ag/AgCl reference electrode and a graphite rod counter electrode. A 0.1 M KOH aqueous solution served as the electrolyte, which was purged with nitrogen for 30 min before testing. Polarization performance and stability tests were conducted on the CHI 900D workstation. Linear sweep voltammetry (LSV) was conducted from −1 to −2 V vs Ag/AgCl at a rate of 5 mV/s while rotating at 1600 rpm. All LSV curves were iR-corrected. Stability was evaluated through chronopotentiometry at a constant current density of 10 mA/cm^2. Double-layer capacitance (Cdl) was determined using the BioLogic VSP potentiostat by collecting cyclic voltammetry data within a non-Faradaic window of 0.2–0.3 V vs. Ag/AgCl at scan rates between 40 and 100 mV/s. Cdl was determined from the linear relationship between current density and scan rate at 0.25 V. All measured potentials were converted to the RHE using:

$$E_{RHE} = E_{Ag/AgCl} + 0.198 + 0.059 \times pH \quad (1)$$

2.4 | Characterizations

X-ray powder diffraction (XRD) was performed using Empyrean (PANanalytical) with Cu Kα radiation (λ = 1.5406 Å) at 40 kV and 40 mA, collecting data across 2θ = 10°–90°. X-ray photoelectron spectroscopy (XPS), along with valence band X-ray photoelectron spectroscopy (VB XPS), was performed on Axis Ultra DLD, equipped with a monochromatic Al Kα X-ray source. High-resolution imaging was performed using a high-resolution transmission electron microscope (HR-TEM, JEOL JEM-2010F). The morphology of perovskite particles was analyzed using scanning electron microscopy (SEM) with a JSM-6700F System. Inductively coupled plasma mass spectrometry (ICP-MS) analysis was performed with an Agilent 7700 instrument. Fourier Transform Infra-Red spectroscopy (FTIR) was conducted on a Bruker Vertex 70 Hyperion 1000 instrument. Electron Energy Loss Spectroscopy (EELS) was tested on Thermo Fisher Titan Themis G2 300.

2.5 | Computational Details

The bulk structure of orthorhombic $NdFeO_{3-\delta}$ was obtained from the Materials Project, while the structures of $Nd_xBa_{2-x}Fe_2O_{6-\delta}$

16146840, 2026, 14, Downloaded from https://advanced.onlinelibrary.wiley.com/doi/10.1002/aenm.202503486 by Universitaet Bayreuth, Wiley Online Library on [28/07/2026]. See the Terms and Conditions (https://onlinelibrary.wiley.com/terms-and-conditions) on Wiley Online Library for rules of use; OA articles are governed by the applicable Creative Commons License

were generated using the Supercell program using a 2 × 2 × 2 supercell approach [25]. The Supercell program analyzed and produced all possible configurations after merging the symmetrical-equivalent configurations. The generated configurations were then determined by density functional theory (DFT), which was conducted using Vienna Ab initio Simulation Package (VASP). The projector augmented wave pseudopotentials, spin polarization, and the Perdew, Burke, and Ernzerhof functional level of theory, within the generalized gradient approximation scheme for electron exchange-correlation, were used. The strongly correlated Fe-3d electrons were simulated using the DFT+U approach, with the U_{eff} value set at 5.3 eV, consistent with the Materials Project, and have been widely utilized for Fe-based perovskites [26–28]. The energy cutoff for the plane-wave basis set was 450 eV. The Brillouin zone was sampled using a 3 × 3 × 3 Monkhorst-Pack *k*-point mesh for the supercell. The Broyden method was employed for structural relaxation, with convergence criteria of 0.02 eV/Å and 10^{-5} eV for the force and energy, respectively.

To investigate HER energetics, slab models were constructed based on the experimentally observed (110) surface, incorporating a 15 Å vacuum layer along the *c* direction to prevent periodic image interactions. The hydrogen adsorption free energy was calculated as follows [29]:

$$\Delta G = \Delta E + \Delta ZPE - T\Delta S \quad (2)$$

where ΔE represents the DFT-calculated electronic energy change for the hydrogen adsorption step, ΔZPE accounts for zero-point energy corrections of the H adsorbate, T denotes temperature, and ΔS represents entropy changes for the HER step.

2.6 | AFME Fabrication and Operation

The frame of the custom AFME cell (with illustrative schematics shown in Figure 4b; Figures S14–S16) was built from PMMA using laser cutting, while the gasket was made from rubber. The various frames were tightened mechanically to ensure a proper seal with the gasket. A two-channel peristaltic pump (Kamoer) delivered a 1 M KOH electrolyte to the two inlets of the AFME at a constant flow rate of 200 mL/min. For catalyst loading, a 2 mm-thick layer of Ni foam (areal density 350 g/m^2) was utilized. The catalyst ink was prepared by ultrasonically mixing 10 mg of perovskite powder, 10 mg of Vulcan XC-72, 200 µL of Nafion solution (5 wt. %), and 900 µL of ethanol. This catalyst ink was subsequently applied to the Ni foam with a catalyst loading of 2 mg/cm^2 by drop casting (Figure S17). The electrode was then placed in a vacuum oven at 80°C overnight to ensure complete drying. Electrochemical characterization was conducted using a Biologic SP-300 potentiostat.

3 | Results and Discussion

3.1 | Catalyst Development

To investigate the impact of Ba substitution, a series of $Nd_xBa_{2-x}Fe_2O_{6-\delta}$ perovskites with varying Nd: Ba ratios (x = 0.4, 0.8, 1.2, and 1.6, denoted as NBF20, NBF40, NBF60, NBF80, respectively) were synthesized and compared with the parent materials $NdFeO_{3-\delta}$ (NF) and $BaFeO_{3-\delta}$ (BF). Room temperature XRD revealed that NF exhibited an orthorhombic structure, while the incorporation of Ba induced a phase transition to a cubic structure. This transition is complete for most compositions (NBF20, NBF40, and NBF60), although NBF80 still retains minor residual peaks associated with the parent orthorhombic phase (Figure 1a). The diffraction peaks for the double perovskites shifted to lower angles compared to pristine NF, and this shift increased with higher Ba content. This indicated the successful partial substitution of smaller Nd ions with larger Ba ions at the A-site, resulting in lattice expansion. (Figure S1). For NBF40, Rietveld refinement analysis (Figure 1b) revealed a cubic phase (*Pm-3m* space group) with lattice parameters a = b = c = 3.94 Å. SEM-EDS composition (Figure 1d) matched the designed stoichiometry.

The HER electrocatalytic activities of the synthesized catalysts were evaluated using a rotating disk electrode (RDE) in N_2-saturated 0.1 M KOH solution (Figure 1c). NBF40 demonstrated superior performance with the lowest overpotential at 10 mA/cm^2 (η_{10} = 325 mV), followed by NBF20 (η_{10} = 387 mV), NBF60 (η_{10} = 457 mV), NBF80 (η_{10} = 525 mV), NF (η_{10} = 577 mV), and BF (η_{10} = 579 mV). All catalysts exhibit Tafel slopes exceeding 120 mV/dec (Figure S2), indicating the Volmer step remains the rate-determining step. Notably, NBF40 shows the lowest Tafel slope, confirming that Ba substitution successfully accelerates the reaction kinetics. We further evaluated NBF40's HER performance in 1 M KOH and compared it with other Fe-based, Co-based perovskite catalysts and Pt/C benchmark under the same testing conditions [7, 8, 10–13, 30–35] (Figure S3 and Table S1). In 1 M KOH, NBF40 exhibited an onset potential of 46 mV (defined at 1 mA/cm^2) and η_{10} of 184 mV, ranking it the highest-performing Fe-based perovskites ever reported.

To understand how crystal structure affects the microstructure, the morphologies of the parent single perovskites (NF and BF) and the double perovskite (NBF40) were compared using SEM analysis (Figure 1e). BF exhibited large grains (~2 µm). In contrast, NF had smaller grains (~0.4 µm). Notably, the double perovskite NBF40 had an intermediate morphology with grain sizes similar to those of NF but forming a more porous, interconnected structure. This morphology of NBF40 was even more noticeable at higher magnification (Figure S4).

To evaluate the underlying factors influencing the catalytic performance variations, we first investigated the oxidation states of Fe in the $Nd_xBa_{2-x}Fe_2O_{6-\delta}$ series using XPS. As shown in Figure 2a,b, a clear correlation exists between the A-site cation ratio and the B-site transition metal valence. Specifically, the average Fe oxidation state increases systematically with higher Ba content to maintain charge neutrality when substituting Nd^{3+} with Ba^{2+} (Figure 2a,b; Table S2). Among the compositions, NBF40 exhibits an intermediate Fe valence state, which aligns with the optimal A-site ionic electronegativity value (~2.33) proposed by Guan et al. [36] as a descriptor for HER activity (Figure 2a; Figure S5 and Table S3).

To gain deeper theoretical insights into the electronic structure, we performed DFT calculations to analyze the projected density of states (PDOS) for the $Nd_xBa_{2-x}Fe_2O_{6-\delta}$ series. As summarized

16146840, 2026, 14, Downloaded from https://advanced.onlinelibrary.wiley.com/doi/10.1002/aenm.202503486 by Universitaet Bayreuth, Wiley Online Library on [28/07/2026]. See the Terms and Conditions (https://onlinelibrary.wiley.com/terms-and-conditions) on Wiley Online Library for rules of use; OA articles are governed by the applicable Creative Commons License

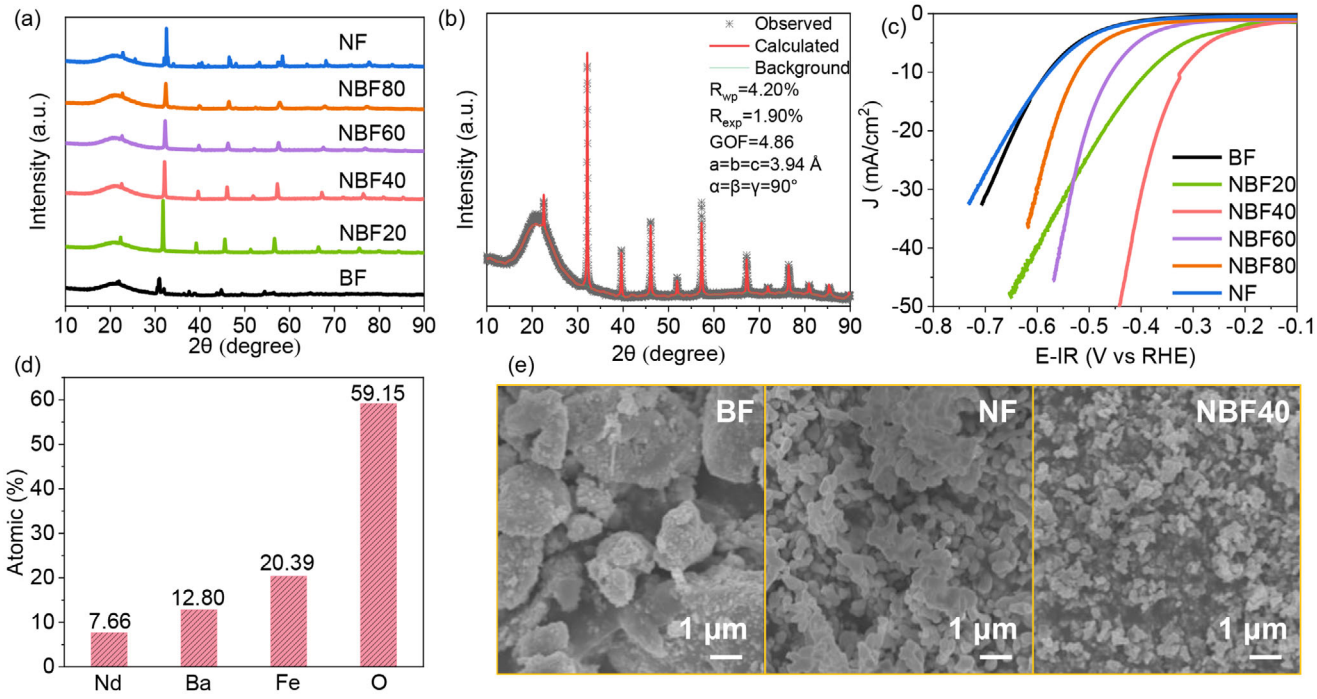

FIGURE 1 | (a) XRD pattern of $Nd_xBa_{2-x}Fe_2O_{6-\delta}$, (b) Refined XRD profiles of the synthesized NBF40, (c) HER polarization profiles of $Nd_xBa_{2-x}Fe_2O_{6-\delta}$, (d) Elemental composition of NBF40, (e) SEM images of BF, NF, and NBF40.

in Figure 2c and Table S4, increasing Ba substitution shifts the occupied states toward the Fermi level, effectively narrowing the bandgap. This reduction in the bandgap enhances electronic conductivity and promotes electron transfer [37]. Experimental VB XPS measurements further corroborate the DFT calculations, showing a shift of occupied states toward the Fermi level of NBF40 compared to NF (Figure S6). However, the improvement in activity was counteracted by the excessive hybridization of the Fe 3d and O 2p orbitals near the Fermi level. While enhancing conductivity, this would create unstable O 2p hole states, detrimental to catalytic activity [38]. NBF40 demonstrates a balanced electronic configuration, suggesting a trade-off bandgap of NBF40.

Crucially, we calculated the hydrogen adsorption free energy (ΔG_H) as a direct catalytic descriptor to study the bonding strength (Figure 2d). The calculations show that NBF40 possesses the near-zero ΔG_H value among the series, indicating an optimal balance between hydrogen adsorption and desorption. In contrast, NBF60 exhibits excessively strong binding, while NBF80 and NBF20 show significantly higher energy barriers for H adsorption. The relation in ΔG_H confirms that the synergistic modulation in NBF40 leads to the most favorable HER energetics.

To evaluate the stability of the NBF40 catalyst, we conducted a chronopotentiometry test at a constant current density of 10 mA/cm^2. As shown in Figure 3a, we observed an interesting "self-improving" behavior, where the potential gradually shifted to more positive values. To study the intrinsic activity variation, we measured the LSV curves (Figure S7) and Cdl (Figure S8) before and after the stability testing, and the current density was subsequently normalized to the electrochemically active surface area (ECSA) to obtain the specific activity. Figure 3b reveals that the specific activity of the post-test sample is higher than that of the pre-test sample, indicating an improvement in the intrinsic activity.

HR-TEM was used to reveal morphological changes in NBF40 during the stability test. (Figure 3c,d). While the pre-test particles exhibited uniform crystalline boundaries (Figure 3c), the post-test sample showed the formation of a distinct amorphous surface layer surrounding the crystalline core (Figure 3d; Figure S9). To understand the chemical driving force behind this restructuring, we monitored electrolyte composition over time using ICP-MS. As shown in Figure 3e, the concentration of Ba ions increased rapidly during the first 10 h and reached a stable plateau thereafter, while Nd and Fe remained negligible. This temporal synchronization between the Ba dissolution kinetics and the performance self-enhancement strongly suggests that the selective leaching of A-site cation is correlated with the "self-improving" behavior. Further analysis by EELS (Figure 3f; Figure S10) confirmed that a portion of Ba is retained within this amorphous layer.

FTIR measurements provided molecular-level evidence for the surface restructuring of NBF40 (Figure 3g). The post-test sample exhibited a new, distinct peak in the 3200–3400 cm^{-1} range, which was absent for the pre-test sample. This peak was characteristic of O—H stretching vibrations, suggesting the formation of surface hydroxyl groups during electrochemical operation. We propose two non-mutually exclusive reasons for the emergence of these hydroxyl groups, both of which were beneficial for HER activity. First, the amorphous layer may facilitate water dissociation (the Volmer step), leading to optimization of the rate-limiting step indicated by the Tafel slope (Figures S2 and S3b). Second, the restructured layer may itself be a hydroxyl-rich oxyhydroxide phase, intrinsically containing a high density of O—H bonds that act as new, highly active catalytic sites. In either scenario, the

16146840, 2026, 14, Downloaded from https://advanced.onlinelibrary.wiley.com/doi/10.1002/aenm.202503486 by Universitaet Bayreuth, Wiley Online Library on [28/07/2026]. See the Terms and Conditions (https://onlinelibrary.wiley.com/terms-and-conditions) on Wiley Online Library for rules of use; OA articles are governed by the applicable Creative Commons License

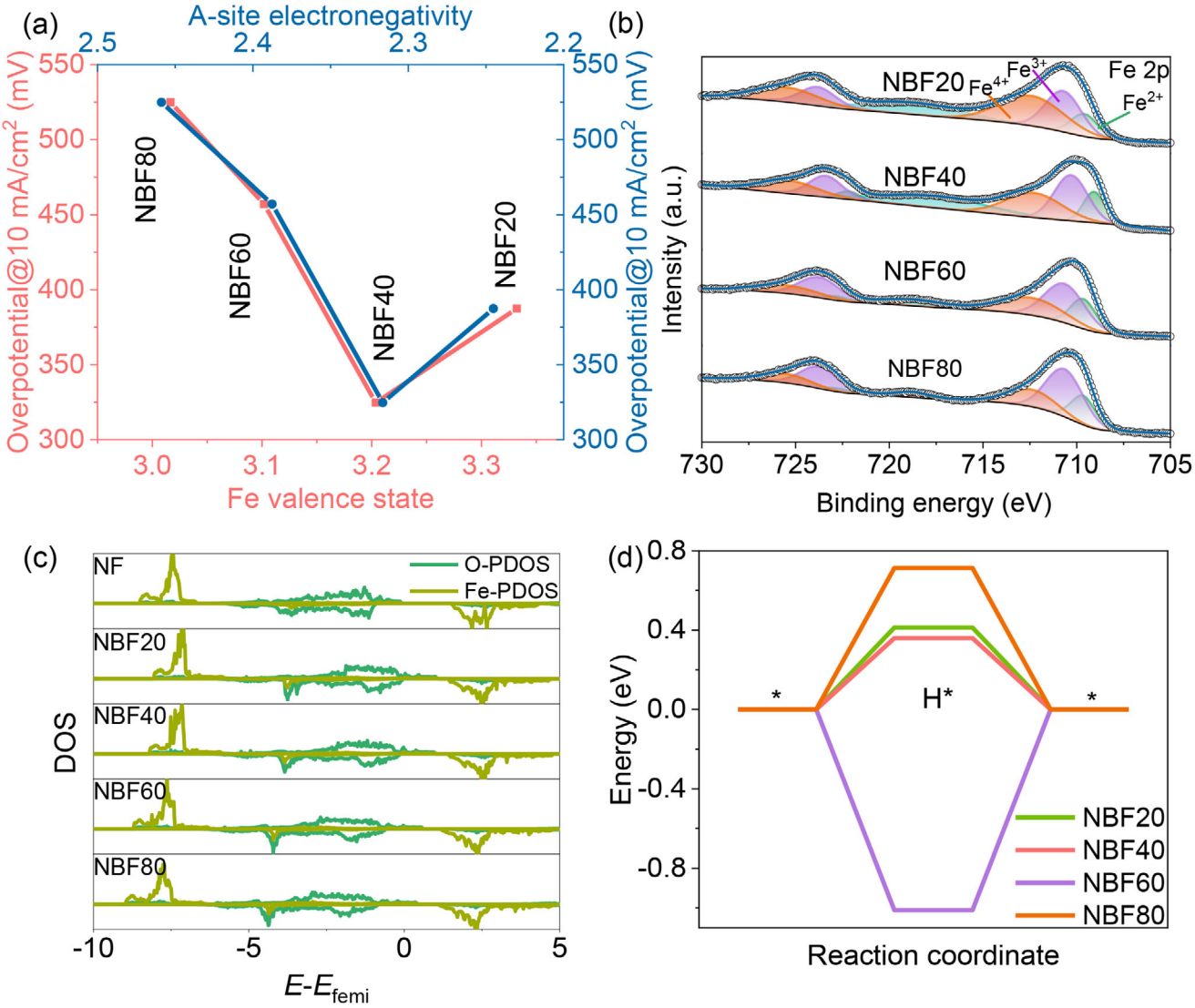

FIGURE 2 | (a) Relationship between HER activities and Fe oxidation states and A-site electronegativity in $Nd_xBa_{2-x}Fe_2O_{6-\delta}$, (b) Fe 2p XPS spectra of $Nd_xBa_{2-x}Fe_2O_{6-\delta}$, (c) Electronic DOS for NF and $Nd_xBa_{2-x}Fe_2O_{6-\delta}$, (d) Calculated Gibbs free energy profiles for hydrogen adsorption on the (110) surfaces of the $Nd_xBa_{2-x}Fe_2O_{6-\delta}$ series.

formation of these hydroxyl functionalities is directly linked to the improved HER performance. To verify the specificity of the restructuring mechanism, the pristine NF was evaluated under identical conditions to the NBF40 (Figures S11–S13). Interestingly, post-test HR-TEM analysis of the NF sample across multiple locations revealed that the surface retained a crystalline nature with visible lattice fringes (Figures S12 and S13), and no amorphous layer was observed. These observations suggest that the in situ amorphization driven by Ba leaching is a unique process characteristic of the Ba-containing NBF40.

3.2 | AFME Application

To evaluate the performance of NBF40 in a practical device, a custom-built, flow-through membrane-less electrolyzer (AFME) was constructed (Figure 4a). In this system, pressurized electrolyte was pumped via two inlets into a central flow channel, where the streams converged and passed through a porous electrode that facilitated simultaneous oxygen and hydrogen evolution. The resulting gas-liquid mixture was then transported to a separator before the electrolyte was recirculated. As detailed in Figure 4b, the cell comprised a central section, which housed the inlets, a 1 mm thick flow channel to minimize ohmic resistance, the porous electrode, and a current collector, which was flanked by two side sections for gas-liquid separation. Rubber gaskets ensured a gas-tight seal between the components. Detailed schematics and photographs are available in Figures S14–S16.

A key consideration for the AFME is the mechanical stability of the catalyst under continuous electrolyte flow. Therefore, we investigated catalyst loading methods, comparing drop casting with air drying and drop casting with vacuum drying under a constant electrolyte washing test. Mass loss measurements (Table S5) confirmed that drop casting followed by vacuum drying provided superior adhesion with no catalyst loss compared to air drying. Based on these results, we further optimized the ink

16146840, 2026, 14, Downloaded from https://advanced.onlinelibrary.wiley.com/doi/10.1002/aenm.202503486 by Universitaet Bayreuth, Wiley Online Library on [28/07/2026]. See the Terms and Conditions (https://onlinelibrary.wiley.com/terms-and-conditions) on Wiley Online Library for rules of use; OA articles are governed by the applicable Creative Commons License

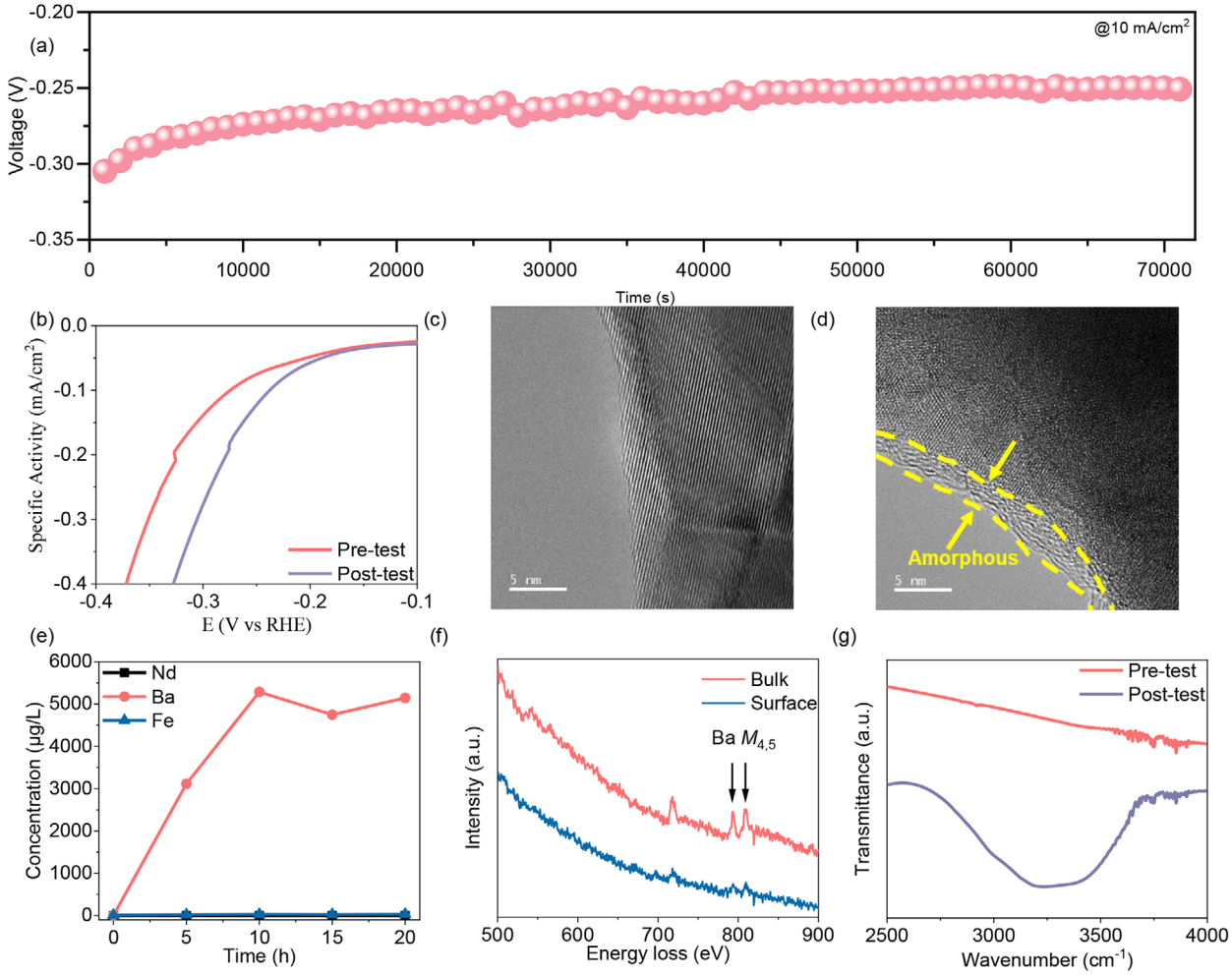

FIGURE 3 | Surface restructuring during electrochemical operation enhanced the stability and activity of NBF40. (a) Chronopotentiometry testing at 10 mA/cm^2 showing self-improving behavior, (b) ECSA-normalized specific activity, confirming the significant enhancement in intrinsic activity, (c,d) High-resolution TEM images revealed the formation of an amorphous surface layer after electrochemical operation, contrasting with the uniform crystalline structure visible before testing, (e) Time-resolved ICP-MS analysis of Nd, Ba, and Fe ion concentrations, demonstrating the selective and rapid dissolution kinetics of Ba, (f) EELS spectra for the bulk and surface regions, indicating the retention of Ba cations within the restructured amorphous phase, (g) FTIR spectra revealed O—H bond formation (3200–3400 cm^{-1}) after electrochemical operation, indicating oxyhydroxide species formation during surface restructuring.

formulation by doubling the Nafion content to ensure sufficient mechanical robustness of the catalyst layer under continuous electrolyte flow during the 1000 h AFME stability test. As a result, the catalyst layer was preserved on the Ni foam substrate, even after a 1000 h stability test (Figure S17).

For performance testing in the AFME, NBF40 on Ni foam was used as the cathode, while an anode was prepared using our previously reported NBFN ($Nd_{0.8}Ba_{1.2}Fe_{1.6}Ni_{0.4}O_{6-\delta}$) perovskite [39], also on Ni foam. The complete NBFN-NBF40 electrolyzer achieved a current density of 50 mA/cm^2 at a cell voltage of 1.93 V without i-R correction (Figure 4c). This performance surpasses that of previously reported flow-through systems, which require 2.59 V [40], and flow-by systems, which need approximately 2.25 V [15] for similar operations. Furthermore, the system demonstrated exceptional long-term stability, maintaining continuous operation for 1000 h with a minimal decay rate of 0.25 mV/h (Figure 4d). This durability established a new benchmark for membrane-less electrolyzers, significantly exceeding the longest previously reported test of 250 h [24]. Such extended stability was critical for practical evaluation, a step often omitted in recent literature [17, 18, 22, 23]. In stark contrast, an electrolyzer using reference NF-loaded electrodes exhibited both inferior performance and rapid degradation under the same conditions. HR-TEM was then used to confirm the crystallinity and restructuring depth of NBF40 after the 1000 h stability test on AFME, as shown in Figure 4d. The crystal matrix was preserved with no collapse or distortion, and the amorphous layer became thicker due to the longer time of the stability test.

4 | Conclusions

In this study, we designed and synthesized the Fe-based double perovskite NBF40, a high-performance catalyst for HER. Through strategic Ba substitution, the catalyst's electronic structure was optimized, resulting in an excellent initial overpotential of 184 mV at 10 mA/cm^2 in 1 M KOH, which ranks it among

16146840, 2026, 14, Downloaded from https://advanced.onlinelibrary.wiley.com/doi/10.1002/aenm.202503486 by Universitaet Bayreuth, Wiley Online Library on [28/07/2026]. See the Terms and Conditions (https://onlinelibrary.wiley.com/terms-and-conditions) on Wiley Online Library for rules of use; OA articles are governed by the applicable Creative Commons License

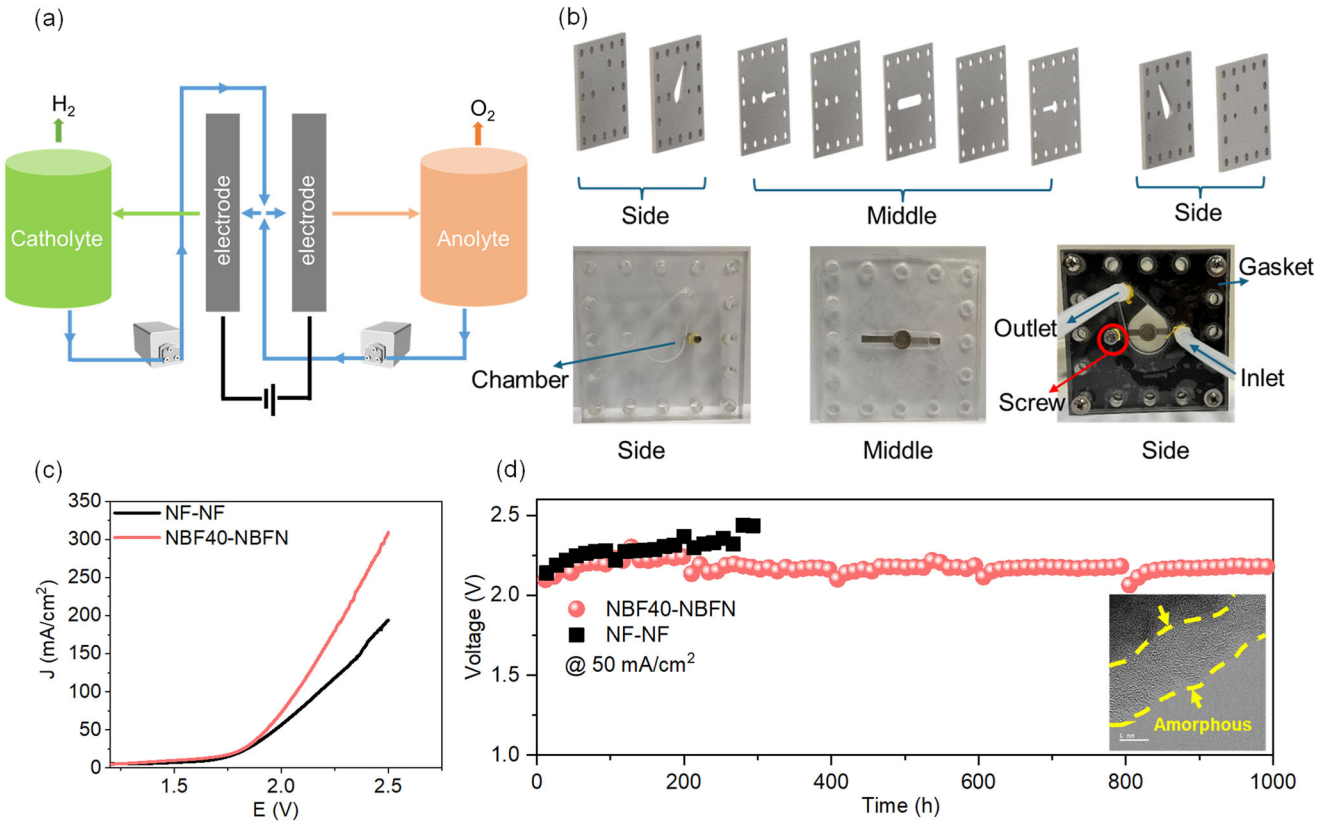

FIGURE 4 | (a) Schematic diagram of the AFME, illustrating the electrolyte flow paths, porous electrode, and gas-liquid separation, (b) Exploded-view diagram and photograph of the AFME cell, detailing its three-section construction and 1 mm flow channel, (c) Polarization curves comparing the NBFN-NBF40 and reference NF-NF electrodes, showing that the NBFN-NBF40 cell achieves 50 mA/cm^2 at a voltage of 1.93 V, (d) Long-term chronopotentiometry data for the NBFN-NBF40 electrodes, demonstrating stable operation for 1000 h with a low decay rate of 0.25 mV/h (insert is HR-TEM image of NBF40 after 1000 h stability test on AFME, showing crystallinity and restructuring depth).

the best Fe-based perovskite catalysts reported (see Table S1 for comparison).

The key innovation is the catalyst's ability to harness an element leaching phenomenon for in situ activation. During operation, the material formed an amorphous surface layer that enhanced its catalytic activity. The practical viability of NBF40 was validated by integrating it into a custom-built AFME. The complete device achieved a current density of 50 mA/cm^2 at a cell voltage of 1.93 V. Furthermore, the system demonstrated unprecedented long-term durability, maintaining stable performance for 1000 h with a minimal decay rate of 0.25 mV/h. This stability far exceeds any previously reported for membrane-less electrolyzer systems.

The combination of high activity, a unique self-improving stability mechanism, and proven device performance creates a clear pathway for producing cost-effective hydrogen from earth-abundant materials.

Acknowledgements

The authors gratefully acknowledge the support of the Hong Kong Research Grant Council (16201622) and Green Tech Fund (GTF202020131). F.C. thanks the University of Bayreuth and the Bavarian Center for Battery Technology (BayBatt) for providing start-up funds. Y. Wang acknowledges the support from the RGC Junior Research Fellow Scheme (JRFS2526-6S08). The authors are grateful to the Materials Characterization and Preparation Facility (MCPF) of the Hong Kong University of Science and Technology for their assistance in experimental characterizations. The authors would like to thank HKUST Fok Ying Tung Research Institute and the National Supercomputing Center in Guangzhou Nansha sub-center for providing high-performance computational resources. Y.S. gratefully acknowledges the support of the Program for Jiangsu Specially Appointed Professors (No. 54901058).

Open access funding enabled and organized by Projekt DEAL.

Conflicts of Interest

The authors declare no conflicts of interest.

Data Availability Statement

The data that support the findings of this study are available from the corresponding author upon reasonable request.

References

1. J. Huang, M. Hao, B. Mao, L. Zheng, J. Zhu, and M. Cao, "The Underlying Molecular Mechanism of Fence Engineering to Break the ActivityStability Trade-Off in Catalysts for the Hydrogen Evolution Reaction," *Angewandte Chemie International Edition* 61 (2022): 202114899.

2. D.-H. Ha, B. Han, M. Risch, et al., "Activity And Stability Of Cobalt Phosphides For Hydrogen Evolution Upon Water Splitting," *Nano Energy* 29 (2016): 37–45, https://doi.org/10.1016/j.nanoen.2016.04.034.

16146840, 2026, 14, Downloaded from https://advanced.onlinelibrary.wiley.com/doi/10.1002/aenm.202503486 by Universitaet Bayreuth, Wiley Online Library on [28/07/2026]. See the Terms and Conditions (https://onlinelibrary.wiley.com/terms-and-conditions) on Wiley Online Library for rules of use; OA articles are governed by the applicable Creative Commons License

3. M. Schalenbach, F. D. Speck, M. Ledendecker, et al., "Nickel-Molybdenum Alloy Catalysts For The Hydrogen Evolution Reaction: Activity And Stability Revised," *Electrochimica Acta* 259 (2018): 1154–1161, https://doi.org/10.1016/j.electacta.2017.11.069.

4. W. Zhai, Y. Ma, D. Chen, J. C. Ho, Z. Dai, and Y. Qu, "Recent Progress on the Long-Term Stability of Hydrogen Evolution Reaction Electrocatalysts,"*InfoMat* 4 (2022): 12357.

5. S. She, Y. Zhu, X. Wu, et al., "Realizing High And Stable Electrocatalytic Oxygen Evolution For Iron-Based Perovskites By Co-Doping-Induced Structural And Electronic Modulation," *Advanced Functional Materials* 32 (2022): 2111091, https://doi.org/10.1002/adfm.202111091.

6. J. Wang, S. Choi, J. Kim, S. W. Cha, and J. Lim, "Recent Advances of First d-Block Metal-Based Perovskite Oxide Electrocatalysts for Alkaline Water Splitting,"*Catalysts* 10 (2020): 770.

7. Y. Zhu, W. Zhou, Y. Zhong, et al., "A Perovskite Nanorod as Bifunctional Electrocatalyst for Overall Water Splitting," *Advanced Energy Materials* 7 (2017): 1602122, https://doi.org/10.1002/aenm.201602122.

8. X. Xu, Y. Chen, W. Zhou, et al., "A Perovskite Electrocatalyst for Efficient Hydrogen Evolution Reaction," *Advanced Materials* 28 (2016): 6442–6448, https://doi.org/10.1002/adma.201600005.

9. Z. Zhang, Y. Chen, Z. Dai, S. Tan, and D. Chen, "Promoting Hydrogen-Evolution Activity And Stability Of Perovskite Oxides Via Effectively Lattice Doping Of Molybdenum," *Electrochimica Acta* 312 (2019): 128–136, https://doi.org/10.1016/j.electacta.2019.04.163.

10. P. Ilanchezhiyan, G. M. Kumar, C. Siva, T. W. Kang, and D. Y. Kim, "$SmFeO_3$ and $SmFe_{1-x}Er_xO_3$ Based Perovskite Nanorods For Improved Oxygen And Hydrogen Evolution Functions," *International Journal of Energy Research* 45 (2021): 3955–3965, https://doi.org/10.1002/er.6049.

11. J. Dai, Y. Zhu, Y. Zhong, et al., "Enabling High and Stable Electrocatalytic Activity of Iron-Based Perovskite Oxides for Water Splitting by Combined Bulk Doping and Morphology Designing," *Advanced Materials Interfaces* 6 (2019): 1801317, https://doi.org/10.1002/admi.201801317.

12. J. Gao, Y. Zhang, X. Wang, et al., "Nitrogen-Doped $Sr_2Fe_{1.5}Mo_{0.5}O_{6-\delta}$ Perovskite As An Efficient And Stable Catalyst For Hydrogen Evolution Reaction," *Materials Today Energy* 20 (2021): 100695, https://doi.org/10.1016/j.mtener.2021.100695.

13. S. B. Karki, A. N. Andriotis, M. Menon, and F. Ramezanipour, "Bifunctional Water-Splitting Electrocatalysis Achieved by Defect Order in LaA_2 Fe_3O_8 (A = Ca, Sr)," *ACS Applied Energy Materials* 4 (2021): 12063–12066, https://doi.org/10.1021/acsaem.1c02028.

14. G. D. O'Neil, C. D. Christian, D. E. Brown, and D. V. Esposito, "Hydrogen Production with a Simple and Scalable Membraneless Electrolyzer"*Journal of The Electrochemical Society* 163 (2016): F3012.

15. S. M. H. Hashemi, M. A. Modestino, and D. Psaltis, "A Membrane-Less Electrolyzer for Hydrogen Production Across the pH Scale,"*Energy & Environmental Science* 8 (2015): 2003–2009.

16. X. Pang, J. T. Davis, A. D. Harvey, and D. V. Esposito, "Framework For Evaluating The Performance Limits Of Membraneless Electrolyzers," *Energy & Environmental Science* 13 (2020): 3663–3678, https://doi.org/10.1039/D0EE02268C.

17. P. Hadikhani, S. M. H. Hashemi, S. A. Schenk, and D. Psaltis, "A Membrane-Less Electrolyzer With Porous Walls For High Throughput And Pure Hydrogen Production," *Sustainable Energy & Fuels* 5 (2021): 2419–2432, https://doi.org/10.1039/D1SE00255D.

18. G. Yang, S. Yu, Y. Li, et al., "A Simple Convertible Electrolyzer In Membraneless And Membrane-Based Modes For Understanding Water Splitting Mechanism," *Journal of Power Sources* 487 (2021): 229353, https://doi.org/10.1016/j.jpowsour.2020.229353.

19. J. T. Davis, J. Qi, X. Fan, J. C. Bui, and D. V. Esposito, "Floating Membraneless PV-Electrolyzer Based On Buoyancy-Driven Product Separation," *International Journal of Hydrogen Energy* 43 (2018): 1224–1238, https://doi.org/10.1016/j.ijhydene.2017.11.086.

20. J. Mahanta, S. Gupta, P. R. Parmar, et al., "Nanoplasmonic Microfluidic Electrolyzer for Membraneless Hydrogen Production," *Energy & Fuels* 38 (2024): 15701–15713, https://doi.org/10.1021/acs.energyfuels.4c02131.

21. B. Samir De, J. Cunningham, N. Khare, J.-L. Luo, A. Elias, and S. Basu, "Hydrogen Generation And Utilization In A Two-Phase Flow Membraneless Microfluidic Electrolyzer-Fuel Cell Tandem Operation For Micropower Application," *Applied Energy* 305 (2022): 117945, https://doi.org/10.1016/j.apenergy.2021.117945.

22. R. Borah, K. Raj A G, and S. W. Verbruggen, "Flow-By Membraneless Electrolyzer Designs: A Macroporous Flow Dividing Mesh Enhances Maximum Allowable Electrode Length," *Fuel* 377 (2024): 132779, https://doi.org/10.1016/j.fuel.2024.132779.

23. M. I. Gillespie, F. van der Merwe, and R. J. Kriek, "Performance Evaluation Of A Membraneless Divergent Electrode-Flow-Through (DEFT) Alkaline Electrolyser Based On Optimisation Of Electrolytic Flow And Electrode Gap," *Journal of Power Sources* 293 (2015): 228–235, https://doi.org/10.1016/j.jpowsour.2015.05.077.

24. M. I. Gillespie and R. J. Kriek, "Hydrogen Production From A Rectangular Horizontal Filter Press Divergent Electrode-Flow-Through (DEFT™) Alkaline Electrolysis Stack," *Journal of Power Sources* 372 (2017): 252–259, https://doi.org/10.1016/j.jpowsour.2017.10.080.

25. K. Okhotnikov, T. Charpentier, and S. Cadars, "Supercell Program: A Combinatorial Structure-Generation Approach For The Local-Level Modeling Of Atomic Substitutions And Partial Occupancies In Crystals," *Journal of Cheminformatics* 8 (2016): 17, https://doi.org/10.1186/s13321-016-0129-3.

26. Y. Wang, Z. Wang, K. Yang, et al., "Self-Recoverable Symmetric Protonic Ceramic Fuel Cell With Smart Reversible Exsolution/Dissolution Electrode," *Advanced Functional Materials* 34 (2024): 2404846, https://doi.org/10.1002/adfm.202404846.

27. Z. Wang, Y. Wang, J. Wang, et al., "Rational Design Of Perovskite Ferrites As High-Performance Proton-Conducting Fuel Cell Cathodes," *Nature Catalysis* 5 (2022): 777–787, https://doi.org/10.1038/s41929-022-00829-9.

28. A. Tahir, Y. Wang, J. Li, Y. Tian, and F. Ciucci, "Accelerated Discovery of High-Performance PCFC Cathodes: Computational-Experimental Optimization of Cobalt-Substituted $Ba_{0.95}La_{0.05}FeO_{3-\delta}$," *Advanced Functional Materials* 35 (2025): 2506489, https://doi.org/10.1002/adfm.202506489.

29. J. K. Nørskov, T. Bligaard, A. Logadottir, et al., "Trends in the Exchange Current for Hydrogen Evolution,"*Journal of The Electrochemical Society* 152 (2005): J23.

30. W. Zhang, M. Xue, X. Zhang, et al., "Boosting Oxygen/Hydrogen Evolution Catalysis Via Ruthenium Doping In Perovskite Oxide For Efficient Alkaline Water Splitting," *Applied Surface Science* 664 (2024): 160278, https://doi.org/10.1016/j.apsusc.2024.160278.

31. S. Li, T. Xia, Y. Dou, et al., "Phosphatizing Engineering of Perovskite Oxide Nanofibers for Hydrogen Evolution Reaction to Achieve Extraordinary Electrocatalytic Performance," *Advanced Functional Materials* 32 (2022): 2112164, https://doi.org/10.1002/adfm.202112164.

32. S. Lai, K. Li, X. Lv, et al., "Molybdenum-Tailored Perovskite Oxides For Efficient Electrocatalytic Hydrogen Evolution Via B-Site Engineering In Alkaline Media," *Journal of Power Sources* 630 (2025): 236089, https://doi.org/10.1016/j.jpowsour.2024.236089.

33. X. Yang, T. Xia, Q. Li, et al., "Achieving Highly Active A-Site Cation-Deficient Perovskite Electrocatalysts Operated At Large Current Density Toward Hydrogen Evolution Reaction," *Separation and Purification Technology* 339 (2024): 126715, https://doi.org/10.1016/j.seppur.2024.126715.

34. D. Liu, M. Chen, K. An, et al., "In Situ Surface Reconstruction on $LaCoO_{3-\delta}$ Leads To Enhanced Hydrogen Evolution Reaction," *Journal of Alloys and Compounds* 891 (2022): 161754, https://doi.org/10.1016/j.jallcom.2021.161754.

16146840, 2026, 14, Downloaded from https://advanced.onlinelibrary.wiley.com/doi/10.1002/aenm.202503486 by Universitaet Bayreuth, Wiley Online Library on [28/07/2026]. See the Terms and Conditions (https://onlinelibrary.wiley.com/terms-and-conditions) on Wiley Online Library for rules of use; OA articles are governed by the applicable Creative Commons License

35. J. Song, C. Zhu, B. Z. Xu, et al., "Bimetallic Cobalt-Based Phosphide Zeolitic Imidazolate Framework: CoP x Phase-Dependent Electrical Conductivity and Hydrogen Atom Adsorption Energy for Efficient Overall Water Splitting," *Advanced Energy Materials* 7 (2017): 1601555, https://doi.org/10.1002/aenm.201601555.

36. D. Guan, J. Zhou, Y.-C. Huang, et al., "Screening Highly Active Perovskites For Hydrogen-Evolving Reaction Via Unifying Ionic Electronegativity Descriptor," *Nature Communications* 10 (2019): 3755, https://doi.org/10.1038/s41467-019-11847-w.

37. Z. Shen, M. Qu, J. Shi, et al., "Correlating The Electronic Structure Of Perovskite $La_{1-x}Sr_xCoO_3$ With Activity For The Oxygen Evolution Reaction: The Critical Role of Co 3d Hole State," *Journal of Energy Chemistry* 65 (2022): 637–645, https://doi.org/10.1016/j.jechem.2021.06.032.

38. D. Guan, H. Xu, Q. Zhang, et al., "Identifying a Universal Activity Descriptor and a Unifying Mechanism Concept on Perovskite Oxides for Green Hydrogen Production," *Advanced Materials* 35 (2023): 2305074, https://doi.org/10.1002/adma.202305074.

39. Y. Bi, Y. Wang, Y. Song, Q. Chen, and F. Ciucci, "Achieving High-Performance OER Catalysis With Dual-Site Modulated Fe-Based Perovskites," *Journal of Materials Chemistry A* 13 (2025): 21898–21907, https://doi.org/10.1039/D5TA01754H.

40. A. Badreldin, A. El Ghenymy, A.-R. Al-Zubi, et al., "Stepwise Strategies For Overcoming Limitations Of Membraneless Electrolysis For Direct Seawater Electrolysis," *Journal of Power Sources* 593 (2024): 233991, https://doi.org/10.1016/j.jpowsour.2023.233991.

Supporting Information

Additional supporting information can be found online in the Supporting Information section.

Supporting File: aenm70717-sup-0001-SuppMat.docx.

16146840, 2026, 14, Downloaded from https://advanced.onlinelibrary.wiley.com/doi/10.1002/aenm.202505486 by Universitaet Bayreuth, Wiley Online Library on [28/07/2026]. See the Terms and Conditions (https://onlinelibrary.wiley.com/terms-and-conditions) on Wiley Online Library for rules of use; OA articles are governed by the applicable Creative Commons License